

High velocity impact on a thin (non-Newtonian) fluid layer

B. Veltkamp¹, K.P. Velikov^{1,2} and D. Bonn^{1,†}

¹Van der Waals-Zeeman Institute, Institute of Physics, University of Amsterdam, 1098 XH Amsterdam, The Netherlands

²Unilever Innovation Centre Wageningen, Bronland 14, 6708 WH Wageningen, The Netherlands

(Received 4 May 2022; revised 15 October 2022; accepted 15 October 2022)

During the high velocity impact of an object on a solid covered with a thin fluid layer, a lubricated contact exists within the short time in which the liquid is squeezed out from the contact. This is important for e.g. the grip of shoes on wet surfaces. We experimentally study the squeeze flow of such layers and find that the amount of viscous dissipation determines how much fluid remains in the contact after the kinetic energy of the impacting object is absorbed. For impacts with sufficient amount of kinetic energy, it is possible to completely drain a Newtonian or shear thinning fluid from the contact on a short time scale. Viscoelastic liquids, however, cannot be drained by increasing impact velocity, because of the fluids' elastic tendency to retract back into the contact after rapid squeezing. This explains why the presence of polymeric fluids can lead to extreme slipperiness of surfaces. Furthermore, we show that all our experimental results agree with the predictions given by hydrodynamic theory applied to the fluid flow in the gap.

Key words: lubrication theory, viscoelasticity

1. Introduction

'Slipperiness' is a human assignment to rate the lubricating properties of a given fluid or surface. A sensible idea is that this human perception is related to the physical quantity 'friction', as a slippery fluid generally is associated with not having any grip on the two surfaces the fluid is located between. However, it is not at all trivial to come up with a more precise physical formulation of 'slipperiness'. In fact, it is not even obvious whether events such as, for example, the oil between smooth running gears, the slippery leaves on

† Email address for correspondence: d.bonn@uva.nl

train tracks (Ishizaka, Lewis & Lewis 2017) and humans slipping when stepping on wet surfaces (Lukey, Romano & Salem 2007) have the same physical reason for being slippery.

The slipperiness of leaves on train tracks likely involves some non-Newtonian rheological properties of polysaccharide polymers from the decaying leaves. Polymer solutions have even been investigated for ‘instant banana peel’ riot control (Lukey *et al.* 2007), because a very slippery polymer solution makes all people and vehicles slip. The proposed fluids are low concentration, high molecular weight flexible polymers. Their unique property is that at low concentrations they form solution with a viscosity almost identical to water, yet they are capable of making peoples’ feet lose grip on the wet streets. The goal of this manuscript is to find an explanation for this remarkable case of slipperiness, which is of paramount importance for applications in, for example, the food industry (Kokini 1987; Campanella & Peleg 2002; Deblais *et al.* 2021) or mechanical engineering (Venner & Lubrecht 2000; Hamrock, Schmid & Jacobson 2004).

An important distinction should be made between two different manners in which a contact can be lubricated. On the one hand, a lubricating layer can establish itself between two surfaces due the lift that is generated hydrodynamically as a consequence of parallel motion (Hamrock *et al.* 2004; Bruus 2008; Veltkamp *et al.* 2021; Veltkamp, Velikov & Bonn 2022). In this case, a hydrodynamically steady state is present and the friction is a result of the shearing of the fluid layer. In previous work (Veltkamp *et al.* 2021, 2022) we have analysed this type of flow in detail. It is concluded that, for the relatively gentle flows probed in these studies, the viscosity of the liquids makes the dominant contribution to the generated lift. Furthermore, friction and lift are generated roughly similarly for Newtonian, shear thinning and viscoelastic liquids, hence neither of these two complex properties make a fluid more slippery than a comparable Newtonian fluid in a steady state lubricating flow.

On the other hand, a lubricating layer can exist between two surfaces whilst being squeezed out and thus not being in steady state. This is in fact closer to the case of a foot stepping onto a puddle of liquid. In this flow type, the two surfaces do not necessarily move horizontally with respect to each other, but a vertical downward motion causes fluid flow. When a foot touches a puddle of fluid at high velocity, the fluid will quickly squeeze out of the gap. We will show here that, in spite of the fact that the layer thickness evolves rapidly, a viscoelastic liquid can stabilize the liquid film for longer than a non-viscoelastic liquid, and hence the contact remains lubricated: both surfaces do not physically touch, resulting in the possible slipping of the foot.

We therefore study relatively high velocity impacts of objects on fluids with various different properties. This is in fact a widely studied topic in itself, and can be divided into impact into a large body of fluid (Moghisi & Squire 1981; Akers & Belmonte 2006; de Goede, de Bruin & Bonn 2019) and impact on a thin layer of fluid (Uddin, Marston & Thoroddsen 2002; Ardekani *et al.* 2009; Moss *et al.* 2011). In this manuscript, we focus on the latter, as determining the precise amount of fluid squeezed out of a thin fluid layer is still relatively unexplored terrain. Similarly, there seems to be little research available specifying whether a fluid layer can be completely drained instantly solely by an impact with high kinetic energy, and if so, how fast this impact has to be to achieve this.

2. Experimental set-up

An experimental set-up is built to measure the rate of squeezing for several liquids. The set-up is conceived in a way that is close to a flat-on-flat impact, but with the top surface slightly curved to make the experiment easier and tractable. The bottom surface holds

a puddle of fluid. We drop the piston of mass $m = 0.975$ kg with a spherical bottom with radius of curvature $R = 1.67$ m and a size $r_m = 0.075$ m (see [figure 1a–c](#)). It can be dropped from various heights, ranging from 5 to 100 mm and is fixed in a holder in such a way that it can freely move up and down, but that it is incapable of rotating along its central axis. The sliding friction between the piston axis and its holder is found to be dependent on the sliding velocity of the piston, but it always remains below 5% of the gravitational force and is therefore neglected. Therefore the impact velocity on the fluid ranges from 0.3 to 1.4 m s⁻¹. The set-up in its entirety is fixed tightly onto a breadboard placed on a vibration-damping floor, to reduce any possible vibrations the falling piston could create.

After approximating the spherical surface of the piston by a paraboloid, the gap between piston and reservoir is given by

$$h(r) = h_0 + \frac{r^2}{2R}. \quad (2.1)$$

We will refer to h_0 as the 'central layer thickness', as depicted in [figure 1\(c\)](#). In the literature a more common choice for squeeze flow set-ups consists of a flat upper surface (effectively meaning $R \rightarrow \infty$), which is mathematically simpler to calculate and makes the squeezing process longer, making it easier to measure ([Engmann, Servais & Burbidge 2005](#)). Analyses of squeeze flow beyond the plate–plate geometry exist, but are typically much more cumbersome ([Cox & Brenner 1967](#); [Adams *et al.* 1994](#); [Sherwood 2011](#)). The sphere–flat geometry we use has the advantage of being less sensitive to precise alignment, because even if the position of h_0 is slightly off centre and the piston is slightly tilted, the gap profile given in (2.1) remains equally valid for a sphere-on-flat contact. This observation is important, since the high speed and high force nature of our set-up makes very precise alignment difficult.

Four induction sensors are positioned 1 mm underneath the plastic bottom surface (see [figure 1b](#)). These sensors measure the proximity of the aluminium piston with an accuracy of 1 μm and a readout rate of 380 points per second. The sensors are calibrated by attaching the piston to a tensile tester and moving it towards them (without any fluid present) at a slow, controlled speed of 10 $\mu\text{m s}^{-1}$ until the piston collides with the bottom surface. From this, a relation between induction value measured by a sensor and the central layer thickness h_0 is obtained, where the moment of collision corresponds with a thickness $h_0 = 0$. The average of the four individual sensors values is taken to be the definitive value of h_0 , as presented in the rest of the manuscript. For all central layer thicknesses $h_0 < 2.0$ mm the readout values of the four sensors agree to within 10% of each other, giving confidence that the error on the h_0 -measurement is small.

The amount of fluid in the reservoir is kept constant for each measurement. By assuming that the volume of liquid poured onto the bottom surface spreads evenly into a flat layer, the thickness of the fluid layer X_0 is calculated to be 2.0 ± 0.3 mm. The very viscous fluids take a lot of time to flatten, in which case the puddle is flattened out by a strong airflow. Due to this issue the estimated uncertainty on the value of X_0 is rather large.

Various fluids are tested. Two types of Newtonian fluids are used: polydimethylsiloxane (PDMS) oil and glycerol–water mixtures. The PDMS oil is commercially available in different viscosities and the viscosity of glycerol–water mixtures can be tuned by varying the ratio of the two liquids, as described by [Segur & Oberstar \(1951\)](#). Two polymeric solutions are chosen for their shear thinning properties, without exhibiting prominent other non-Newtonian properties: a solution of 10.0 g l⁻¹ polyethylene oxide (chain length 2×10^6 (PEO 2M)) in water and a solution of 5.0 g l⁻¹ xanthan gum in water.

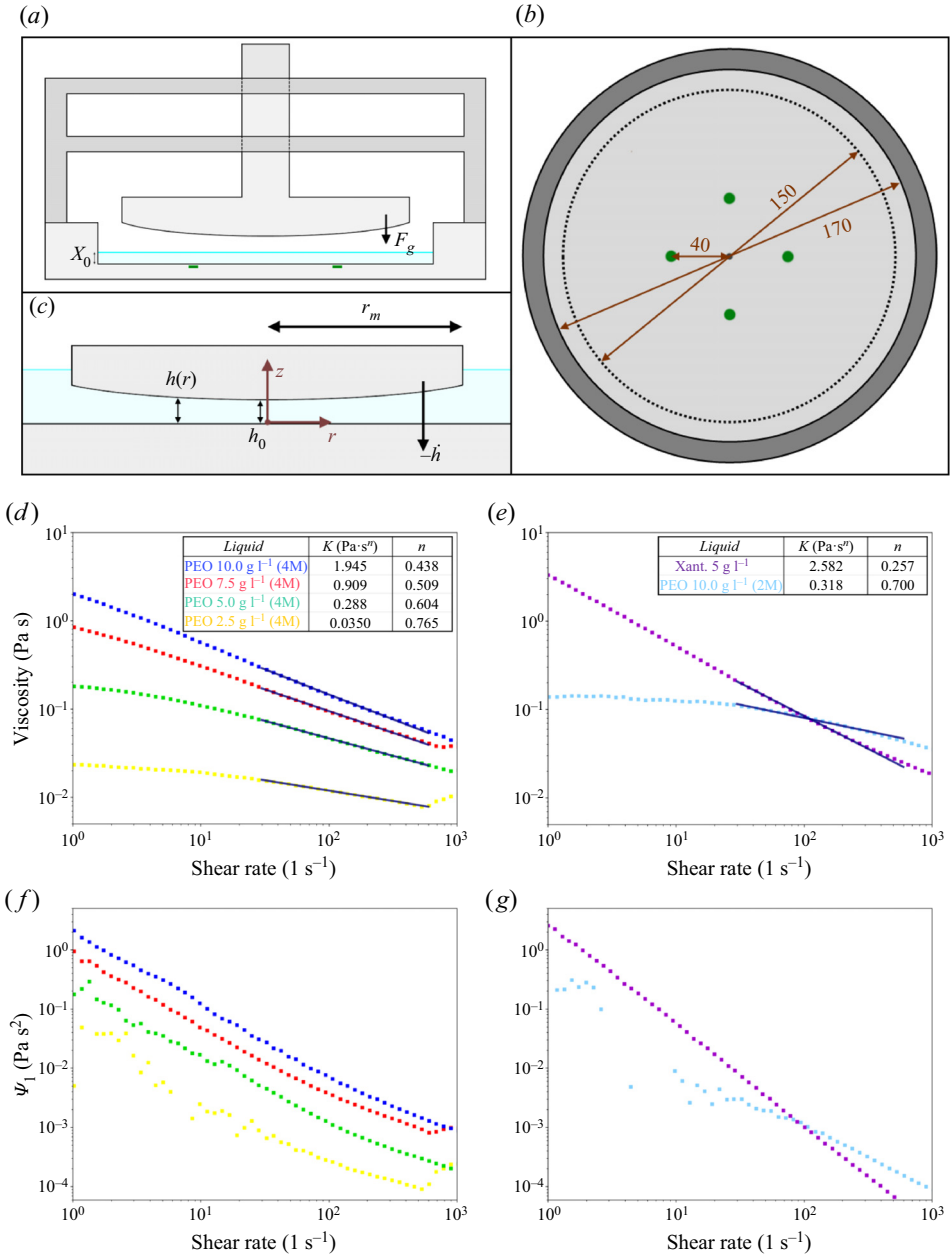


Figure 1. (a) Side view of the experimental set-up, consisting of a surface with curved bottom that can move freely up and down. During experiments it falls down due to gravitational force F_g onto a bottom surface with a thin layer of fluid of thickness X_0 . Green rectangles represent two out of four of the layer thickness measuring induction sensors, positioned 1 mm underneath the surface. (b) Top view of the bottom surface. The green dots indicate the position of the induction sensors underneath the surface. The given distances are in mm. (c) Coordinates system used when the piston is squeezing the liquid layer. The gap size $h(r)$ is given by (2.1). We define h_0 , the layer thickness at $r = 0$, as the 'central layer thickness'. (d,e) Flow curves of the non-Newtonian liquids tested. The dark blue lines indicate a power-law fit according to (2.2) between shear rate $\dot{\gamma} = 30$ and $\dot{\gamma} = 600 \text{ s}^{-1}$, of which the corresponding parameters K and n are displayed in the tables. (f,g) The first-normal-stress coefficient, Ψ_1 , for each of the six liquids as found by the rheometer measurement.

Furthermore, four concentrations of polyethylene oxide (chain length 4×10^6 (PEO 4M)) in water are selected for their viscoelastic properties, ranging from 2.5 to 10.0 g l⁻¹. Prior to the squeezing experiments, the flow profile of all fluids is obtained following standard rheological procedures (Mezger 2006). For all shear-thinning fluids a power-law model was used to describe their viscosity η as a function of shear rate $\dot{\gamma}$

$$\eta(\dot{\gamma}) = K\dot{\gamma}^{n-1}. \tag{2.2}$$

The flow curves together with their corresponding values of the viscosity coefficient K and the power-law index n are shown in figure 1(d,e). The fluids used are from the same batch as we used before (Veltkamp *et al.* 2022). The rheological measurement of the flow curves simultaneously measures the first-normal-stress difference; the first-normal-stress coefficient obtained from these measurements quantifies the elasticity of the polymeric liquids (Bird, Armstrong & Hassager 1987; Mezger 2006); the values are plotted in figure 1(f,g). In principle, there exist more rheological parameters related to the viscoelastic properties of a liquid, such as the extensional viscosity or the elastic modulus, yet for our purposes the first-normal-stress coefficient gives sufficient comparison between the liquids.

3. The forces acting on the impacting surface

In order to predict the development of the layer thickness as a function of time, the upwards force exerted by the fluid onto the piston as a result of the squeezing needs to be calculated. From the lubrication approximation of the Navier–Stokes equations it is possible to obtain an approximate formula for the both the force as a result of viscous dissipation, F_v , and of inertial dissipation, F_i .

A formula for the viscous force of a power-law fluid underneath a parabolic surface has been derived by both Rodin (1996) and Lian *et al.* (2001), after which Meeten (2005) confirmed it experimentally. For these studies the boundary of the piston is assumed to be infinitely far away, which turns out to be a bad approximation for our piston experiment. Therefore, (3.1) for the viscous force with a finite boundary is derived in Appendix A, closely following the steps of Lian *et al.* (2001),

$$F_v = \frac{K(-\dot{h})^n R^{3/2+(1/2)n}}{h_0^{(3/2)n-1/2}} X(s_m). \tag{3.1}$$

Here, \dot{h} is the velocity of the upper surface (which has a negative sign if the piston moves downwards) and $X(s_m)$ a dimensionless function given by (A12) in Appendix A which depends on the boundary proximity parameter

$$s_m = \frac{r_m}{\sqrt{2Rh_0}}. \tag{3.2}$$

This parameter appears naturally as a result of the size of the upper surface being finite. For small layer thickness this plays only a small role, and the assumption $s_m \gg 1$ can be used to substitute $X(s_m)$ by the numerical value $X(s_m \rightarrow \infty)$. However, at a layer thickness h_0 equal to the initial film thickness X_0 , the value of s_m is 0.92, so then the full function $X(s_m)$ must be included. It is important to note that $X(s_m \rightarrow \infty)$ does not exist for $n \leq 1/3$ (Rodin 1996; Lian *et al.* 2001), because in this case the pressure near the edge of the piston contributes more to the net upwards force than the pressure in the central region. Because s_m is finite in our case, we can also use (3.1) for $n \leq 1/3$, yet it must be kept in mind that

the precise location of the edges is important in this case, and that a small misalignment in the set-up will have larger consequences for liquids with strong shear-thinning properties.

The inertial force is calculated by following the same perturbation method as established by Jackson (1963) and later updated by Kuzma (1967). Although the result is strictly speaking only valid for low Reynolds number, it has been found in practice that it works also well for higher Reynolds number (Tichy 1981; Moss *et al.* 2011). After the work of Kuzma, the inertial force has been studied in various other ways, such as configurations with non-parallel plates (Tichy & Modest 1978) and analyses based on a self-similarity approach (Rashidi, Shahmohamadi & Dinarvand 2008). The method by Kuzma (1967) has the advantage that it is relatively easy to implement on a sphere–plate configuration and that one does not have to deal with validity limits, such as is the case for self-similarity approaches (Moss *et al.* 2011). A detailed derivation of (3.3) can be found in Appendix B and yields

$$F_i = -\frac{1}{2}\pi\rho r_m^2 R\ddot{h} + \pi\rho R^2 \dot{h}^2. \quad (3.3)$$

Here, \ddot{h} is the acceleration of the upper surface and ρ the density of the fluid. Because we will only use the inertial force in a theoretical analysis, the assumption $s_m \gg 1$ has already been implemented in (3.3).

Newton’s second law yields the equation of movement for the impacting object

$$m\ddot{h} = F_v + F_i - mg. \quad (3.4)$$

The right-hand side denotes all forces acting on the object, with mg gravitational pull. Four distinct squeeze flow regimes can now be distinguished:

- (i) Slow viscous ($0 = F_v - mg$). This case is characterized by the low velocity and acceleration, so that viscous dissipation dominates over inertial dissipation and the gravitational term in (3.4) is much larger than the acceleration. It is reached only after the initial impact of the piston and it is most commonly the final and longest stage of the squeeze out process. This regime is the most broadly analysed by others for many different types of fluids (Engmann *et al.* 2005). In this regime the kinetic energy of the piston is no longer relevant, whilst the gravitational energy is dissipated by the molecule interactions.
- (ii) Fast inertial squeeze ($m\ddot{h} = F_i$). Here, the inertial force is much larger than the viscous force and the acceleration is much larger than the gravitational one. Hence, in this regime, the gravitational energy can be neglected and the kinetic energy of the piston is transferred into kinetic energy of the fluid particles. The label ‘fast’ is both referring to the object velocity being high and to the rate at which this regime is gone through, since the underlying assumption $\ddot{h} \gg g$ implies that the object acceleration is high. The typical time scale for this type of flow is given by $\bar{t} \equiv X_0/v_0$, with v_0 the impact velocity and X_0 the initial fluid layer. For our experimental parameters it lies within the range $\bar{t} \in [1, 5]$ ms, which is much more rapid than the typical time scale for slow viscous squeezing, which is of the order of seconds for the fluids we used.
- (iii) Fast viscous squeeze ($m\ddot{h} = F_v$). In this situation the viscous force dominates the inertial force and acceleration is much higher than gravity. Similar to case (ii), this regime occurs at the time of impact at a time scale $\bar{t} \equiv X_0/v_0$. The kinetic energy of the piston is dissipated by the viscous interaction within the fluid whilst the kinetic energy of the fluid particles is irrelevant in this regime.

- (iv) Slow inertial squeeze $0 = F_i - mg$. This regime in itself sounds paradoxical, as inertial forces thrive at high velocity, yet it could theoretically exist in specific circumstances, namely when a low-viscosity and high-density fluid is being squeezed from underneath a large surface. For our experimental set-up the regime is never reached, so we will not analyse it here.

The characteristics of the first three regimes are analysed both theoretically as experimentally in the upcoming sections. The main focus shall be on determining what roles the inertial and viscous forces play during the ‘fast’ squeezing stage, what the layer thickness is that the piston settles on after this stage and whether it is possible to completely drain the entire fluid layer within this fast stage.

4. Slow squeeze for Newtonian and shear-thinning fluids

The central layer thickness during Newtonian slow viscous squeeze flow goes asymptotically to zero according to the following exponential decay (Maude 1961; Cox & Brenner 1967):

$$h_0(t) = h_{start} e^{-t/\tau}. \quad (4.1)$$

Here, h_{start} is the starting layer thickness yet to be determined by an earlier squeezing regime, and τ a characteristic time scale in which the slow viscous squeezing occurs, given by

$$\tau = \frac{6\pi\eta R^2}{mg}. \quad (4.2)$$

Experimentally, we retrieve this expected development of the central layer thickness, as the linearity on the lin–log plot (see figure 2a) indeed represents the exponential decay predicted by (4.1). Also, the corresponding values for the time constant τ for several liquids with various viscosities (see figure 2c) agree with (4.2). For power-law liquids the development of the central layer thickness can be derived numerically (see Appendix A), and here too the theory matches well with experimental data (see figure 2d). This agreement in the well-known slow viscous regime gives us confidence to continue our analysis for the lesser known regimes.

As expected, the piston impact velocity plays no role during the slow viscous regime, which is best illustrated by the data depicted in figure 2(a). In this set of experiments, the piston was dropped with various impact velocities onto the same fluid. The only difference between these trials is the difference in the layer thickness h_{start} at which the slow viscous regime begins. After this moment the rest of the squeeze out happens at identical rate for all trials. The exact value of h_{start} and whether it is possible to drain the fluid layer without the slow viscous regime (hence $h_{start} = 0$), is determined by the fast squeezing process happening in the first milliseconds after impact.

5. Fast inertial squeeze

To investigate the effect of inertia on the deceleration of the upper surface, the inertial force given in (3.3) is substituted in the fast inertial approximation of (3.4). This yields a

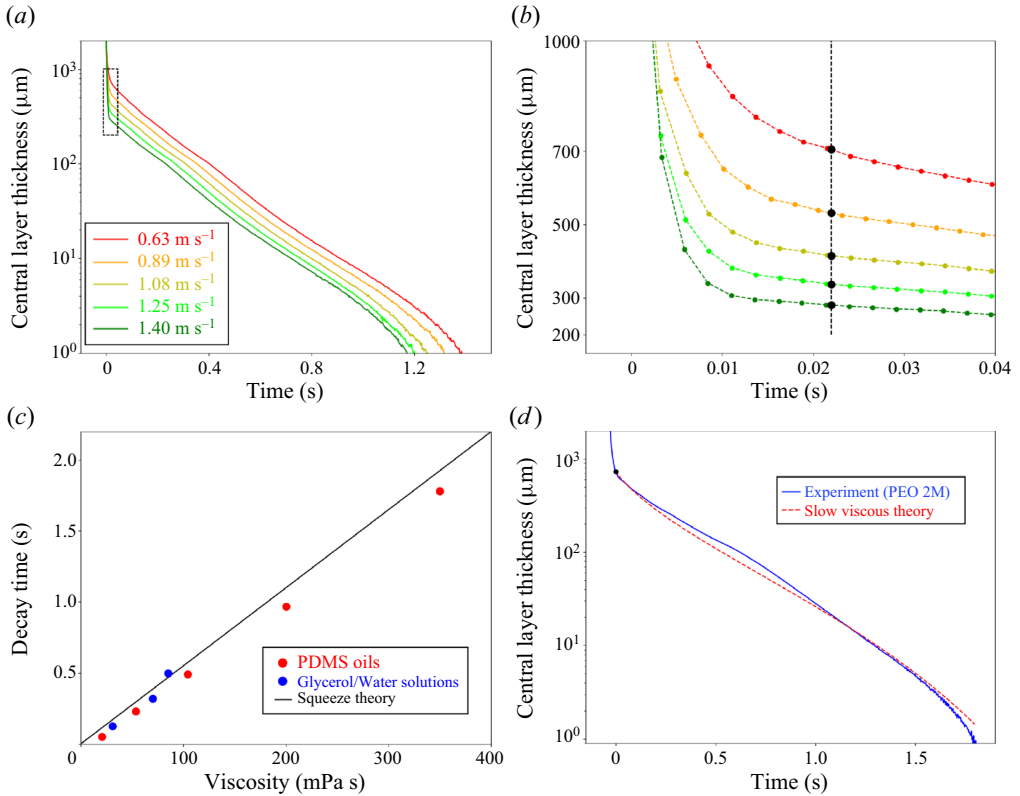


Figure 2. (a) Development of the central layer thickness during the squeeze out of PDMS with $\eta = 53.5 \text{ mPa}\cdot\text{s}$. Impact velocity was varied from 0.63 (red line) to 1.40 m s^{-1} (dark green line) and only has an effect on the squeezing during the moment of impact. The linearity of all the curves (on a lin–log plot) is in agreement with the prediction of exponential decay given in (4.1). (b) The region of the dotted rectangle in (a) zoomed in. The coloured dots are data points measured by the induction sensors, connected by a dotted line for visual guidance. The black dots indicate the layer thickness h_{start} at $t = 22 \text{ ms}$ after impact when the slow viscous regime starts. As explained in the text, the values of h_{start} depend on impact velocity and are later used in the analysis for the fast viscous regime. (c) Values of the characteristic decay time for various viscosities of PDMS oil (red dots) and glycerol–water solutions (blue dots), found by fitting (4.1) to the time vs layer thickness curves, such as those displayed in (a). The black line displays theoretical prediction by (4.2). (d) Comparison between the experimental data of the squeeze out of the non-Newtonian liquid PEO 2M (blue line) and theoretical prediction (dashed red line). The dot indicates the moment chosen for the slow viscous regime to start.

characteristic differential equation for fast inertial squeeze

$$\ddot{h} = \epsilon \frac{\dot{h}^2}{X_0}. \quad (5.1)$$

The parameter ϵ is given by

$$\epsilon \equiv \frac{\beta}{1 + \beta} \frac{1}{s_{m,0}^2}, \quad (5.2)$$

with β defined by

$$\beta \equiv \frac{\pi \rho r_m^2 R}{2m}. \quad (5.3)$$

Here, β is a measure of the ratio of the inertia of the piston vs the inertia of the particles. The limit $\beta \rightarrow \infty$ (and hence $\epsilon \rightarrow s_{m,0}^{-2}$) refers to the situation with particle inertia being much higher than the piston inertia, whereas the opposite limit $\beta \rightarrow 0$ (and therefore $\epsilon \rightarrow 0$) refers to the inverse case.

The parameter $s_{m,0}$ denotes the value of s_m at the moment of first contact between the centre of the piston and the fluid surface. For our experiments we find $s_{m,0} = r_m/\sqrt{2RX_0} = 0.92$. It is assumed that, when $h_0 = X_0$, the surface of the piston is directly fully covered in fluid. Since the surface is slightly curved, the lowest point of the upper surface will be submerged first, whilst the edges follow slightly later. It is not trivial to describe the effect of this gradual submersion on the forces mathematically, yet the assumption made will overestimate the force at the moment the piston is not yet fully covered in liquid. In practice, however, the relevant forces are still small during the stage with a relatively large layer present, so the slight overestimation of the deceleration of the piston can be assumed insignificant.

Apart from the assumption that the surface is instantaneously covered in liquid, the derivation of the inertial force contains several more approximations and assumptions. These consist of the layer thickness being much smaller compared with the piston radius (to make the lubrication approximation valid), the perturbation approximation of Kuzma (1967) stating that flow profile is still similar to the viscous flow profile and the approximation that the edge of the surface is infinitely far away. Without these a more general version of (5.1) could be obtained, yet for simplicity we stick to the current form.

Equation (5.1) is solved exactly provided the initial conditions $h_0(t = 0)$ being equal to the fluid puddle thickness X_0 and $h(t = 0)$ being equal to the impact velocity $-v_0$. The solution reads

$$h_0(t) = X_0 \left(1 - \frac{\log \left(1 + \epsilon \frac{v_0 t}{X_0} \right)}{\epsilon} \right). \tag{5.4}$$

According to (5.2), the value of ϵ is limited between $\epsilon \in [0, 1.18]$, and in figure 3(a) (5.4) is plotted for three values of ϵ within this range. The limit $\epsilon \rightarrow 0$ correlates with the upper surface not experiencing any force and hence reaching the surface within a time $\bar{t} = X_0/V_0$. The other extreme $\epsilon \rightarrow 1.18$ corresponds to a maximized inertial force. A larger ϵ slows down the rate at which the full layer is squeezed out, yet in all cases it reaches zero in finite time. It can therefore be concluded that the inertial force by itself cannot stop the impacting object from reaching the surface. The inertial force thus gives no explanation for the found values of h_{start} in figure 2(b) after which slow viscous squeezing begins.

It must be noted that a different shape of configuration might change this conclusion. Possibly a flat–flat configuration allows for the inertial force to settle the upper surface on a non-zero h_{start} . Theoretically, this geometry can generate a large inertial force as fluid particles flow out of the narrow edges of the gap at high velocity. The formula for inertial force given in Kuzma (1967) can be used to obtain a similar differential equation as our (5.1). Possibly it will predict asymptotic behaviour for the $h_0(t)$ profile, settling on a non-zero h_{start} .

Because the equation for the inertial force is derived using a perturbation method, the given analysis is valid when inertial stresses are less than or roughly equal to viscous stresses, even though it has been found that the method works for large Reynolds number as well (Tichy 1981; Moss *et al.* 2011). It remains unclear what happens when inertial

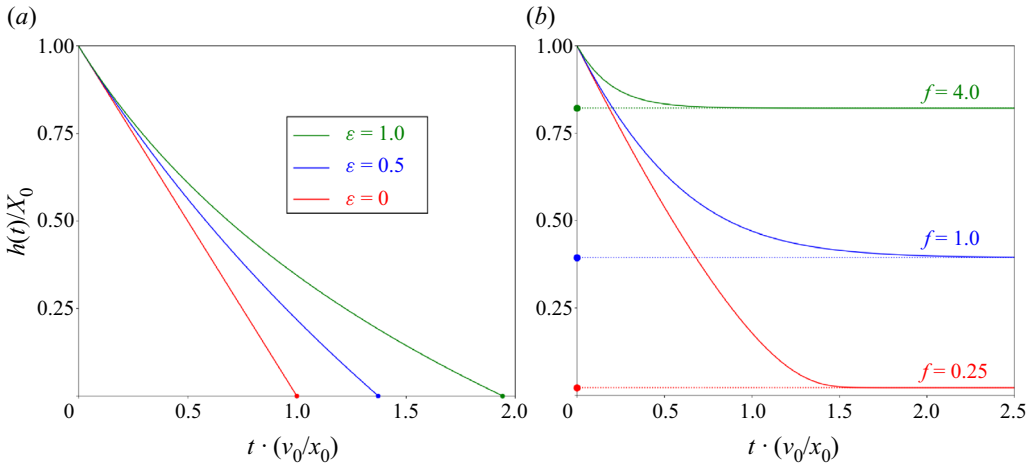


Figure 3. Development of the central layer thickness modelled for fast inertial squeezing (a) and fast viscous squeezing (b). For (a) (5.4) is plotted for three different values of ϵ (as defined in (5.2)), and in all cases the layer thickness reaches zero in finite time, meaning all liquid is squeezed out of the contact when only the inertial force is taken into account. The curves for the fast viscous regime (b) are modelled with $n = 1$ and three different values for the parameter f , as defined in (6.2). In contrast to fast inertial squeezing, the fast viscous squeezing can reach a stable non-zero value for the remaining layer depending on the parameter f , as indicated by the horizontal dotted lines and the dots on the y-axis.

stresses are much larger than viscous stresses, but in the upcoming section we will show that experimental data suggest that only the viscous force is relevant for determining how much fluid is squeezed out by the impact of the piston. The inertial force is irrelevant, which agrees with the analysis by the perturbation method. Therefore, we will not analyse the separate case in which the inertial force is much higher than the viscous force.

6. Fast viscous impact

The characteristic differential equation for fast viscous squeeze is derived in Appendix C and reads

$$\ddot{h}h_0^{(3/2)n-1/2} = (-\dot{h})^n \frac{KR^{3/2+(1/2)n}X(s_m)}{m}. \tag{6.1}$$

From here the parameter f follows, which is defined as

$$f \equiv \frac{KR^{3/2+(1/2)n}X(s_m \rightarrow \infty)X_0^{3/2-(3/2)n}}{mv_0^{2-n}}. \tag{6.2}$$

Together with the power-law index n , the parameter f contains all the physics that determines the flow during fast viscous squeezing. Equation (6.1) cannot be solved exactly, even not for the Newtonian case for which only an implicit solution containing an exponential integral is obtained (Polyanin & Zaitsev 2003), and therefore a numerical approach is provided in Appendix C. Just as in the fast inertial regime, it is assumed that at $h_0 = X_0$ the surface of the piston is fully covered in liquid. It is found that during fast viscous squeeze either a fraction or all of the fluid layer is drained underneath the piston within a time scale of order \bar{t} , depending on values of f and the power-law index n , see figure 3(b). After this, the slow viscous regime driven by gravity takes over. The viscous

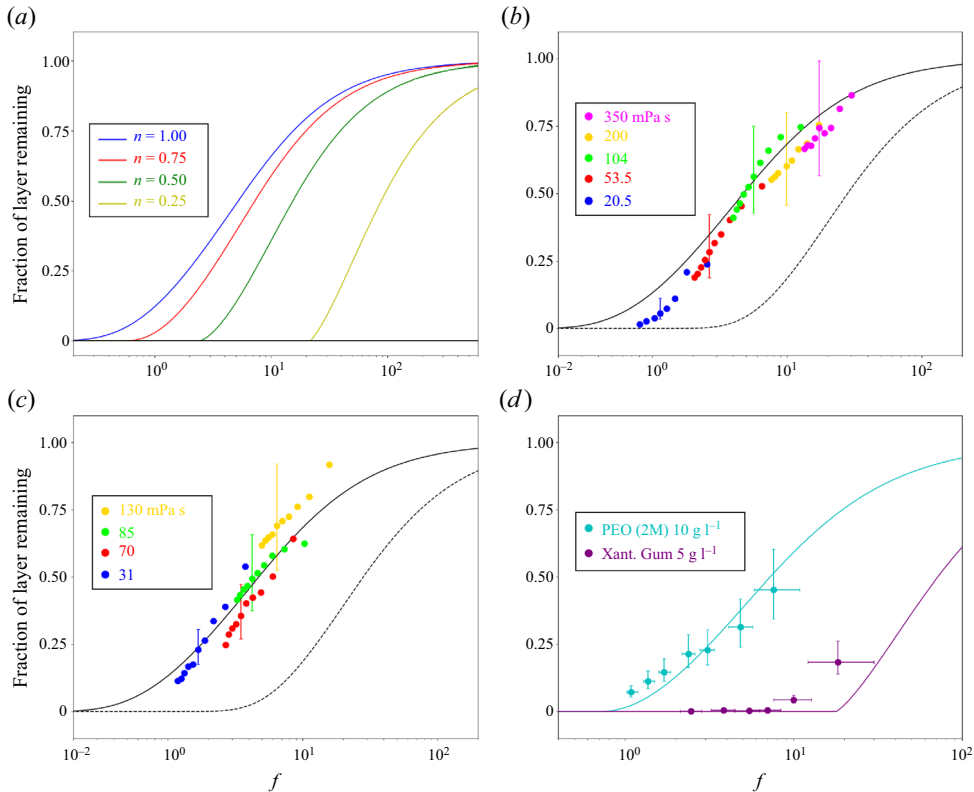


Figure 4. (a) Comparison of the theoretical dependence of the remaining layer thickness as a function of f and n , as calculated in Appendix C. For $n < 1$ a zero layer is predicted for finite values of f , as shown by the coloured dots on the x -axis, whereas for $n = 1$ the curve approaches zero asymptotically. The steepness of the slopes indicates that the more shear thinning a fluid is, the easier it can be squeezed out of a contact by means of increasing the impact velocity. (b,c) The amount of layer remaining in the gap after the fast viscous impact for various viscosities of PDMS oil (b) and glycerol–water solutions (c). The colour of the dots indicates viscosity, and impact velocity was varied to test different values of f (see (6.2)). As further explained in the text, the vertical error bars result from both the uncertainty in the method of finding h_{start} (as displayed in figure 2b) and the uncertainty in initial layer thickness X_0 . Only one error bar is displayed per series of measurements, for clarity purposes. Dots with the same colour have similar errors. The black lines depict the theoretical prediction in a model with only the viscous force included, as shown in Appendix C. The dashed lines depict the same model with inertia also included. By multiplying the ‘fraction of layer remaining’ by the initial layer thickness X_0 the values of h_{start} as depicted in figure 2(b) can be retrieved again. (d) The layer remaining after fast viscous impact for the non-Newtonian liquids PEO 2M (cyan dots) and Xanthan Gum (purple dots). As both liquids have $n \neq 1$, they both have a separate characteristic theoretical line. The horizontal error bars are a result of the uncertainty in X_0 and v_0 whilst calculating f .

force can thus absorb all the kinetic energy of the impacting piston, without the piston reaching the bottom surface, in sharp contrast to the inertial force.

The relation between the remaining fluid layer and the parameters f and n is shown in figure 4(a). For Newtonian liquids (the $n = 1$ curve) the fraction of the initial layer remaining goes asymptotically to zero for small f , meaning that, mathematically speaking, the fluid layer can handle being impacted by a piston with infinitely high velocity and still have an infinitesimal amount of layer remaining.

For shear-thinning liquids, this characteristic of the differential equation is different, and there is a finite f_c below which all fluid is drained in the fast viscous regime, as can be

observed by the kink in all the $n < 1$ curves. In general, the shear-thinning properties of a fluid decrease the resistance that the layer thickness provides against high impact velocity, as becomes evident from the steepness of the curves in figure 4(a). This makes sense physically, as higher impact means higher shear within the fluid, which yields a lower viscosity by the definition of the shear-thinning fluid, which eases the squeezing process.

However, even in the Newtonian case the remaining layer thickness approaches zero for small f , and from a practical point of view, it will eventually reach the size of the surface roughness of both surfaces, after which the surfaces touch. So it can be concluded that the fast viscous regime allows for the fluid underneath the piston to be drained on a fast time scale (of order \bar{t}) in all cases with $n \leq 1$. With the foot analogy discussed in the introduction in mind, this would imply that a sufficiently energetic, high-speed positioning of the foot would in principle be enough to drain the layer within the fast viscous regime and find grip in the surface-on-surface contact created. (We assume the foot is rigid in this analogy, as deformable surfaces might change this conclusion.)

For experimental confirmation of these findings in the fast viscous regime, various fluids were impacted with several different velocities. The fraction of the initial layer remaining was determined by choosing h_{start} at 22 ms after the piston hits the fluid layer, as depicted in figure 2(b), which is a reasonable time scale at least three factors larger than \bar{t} after which the impact of the piston is slowed down to a near standstill and when the slow viscous regime starts. The corresponding value of f was calculated by (6.2) with the given fluid and set-up parameters. The result of this analysis is shown in figure 4(b–d). The ‘fast’ regime transitions into the ‘slow’ regime smoothly, so choosing a single instance for h_{start} as ‘the beginning of slow squeezing’ is somewhat arbitrary. From an analysis point of view, h_{start} should ideally be selected directly after the first rapid deceleration of the piston, before the slow viscous regime has lowered the layer thickness. For consistency, we stick with probing h_{start} at 22 ms, and the vertical error bars show the result for when the probing time is altered to either 12 ms or 32 ms to provide some indication of how much the result depends on this slightly arbitrary choice. The horizontal error bars arrive from the uncertainty in the values of X_0 and v_0 . The experimental findings show good agreement with fast viscous theory. Therefore, it is concluded that viscous dissipation fully determines the amount of liquid being squeezed out during impact.

7. Combined fast viscous and inertial impact

Except for the regimes discussed above, there is apparently another possible approximation. One can include both the inertial and viscous forces in the equation of movement of the impacting object, yielding

$$(m + \frac{1}{2}\pi\rho r_m^2 R)\ddot{h} = \pi\rho R^2 \dot{h}^2 + F_v. \tag{7.1}$$

Using the terminology of Shiffman & Spencer (1945), the term $\frac{1}{2}\pi\rho r_m^2 R \equiv m'$ is defined as the ‘virtual mass’ and represents the inertia of the fluid particles. Despite the real mass of the particles within the gap being much lower than the mass of the piston, the virtual mass can actually be much larger than that of the impacting object, because the particle velocity scales with $\dot{h}(r/h(r))$, where $r/h(r) \gg 1$ in a narrow gap. Note that this directly follows from the conservation of mass underneath the piston and does not depend on the assumptions made for the fluid velocity profile. For our experimental parameters, we find $m' = 15m$, suggesting that the inertia of accelerating and decelerating the fluid particles in the gap actually determines the slow down rate of the piston, instead of the piston mass itself.

Equation (7.1) can be modelled too. Since the fast viscous regime already concluded that inertia itself will not stop the piston, the easiest way of doing this is by taking the results of the fast viscous squeezing and rescaling those by replacing m with $m + m'$. The result of this procedure is plotted as the dashed line in figure 4(b,c). With the virtual mass included, there is no longer agreement between theory and experiments. Perhaps even more curious is that the addition of the inertia in fact results in more liquid being squeezed out, meaning that the inertial force is mainly negative, hence sucking the piston downwards. This discrepancy between model and experimental hints at an error in the interpretation and usage of the inertial force.

Intuitively, one might think that the addition of the extra inertial force would slow down the piston even more, similar to aerodynamic drag. However, the inertial force can become negative, as one of the terms in (3.3) scales with $-\dot{h}$. This is a result found by others (Shiffman & Spencer 1945; Kuzma 1967; Grimm 1976; Usha & Vimala 2002), yet only Shiffman seems to slightly comment on it. In practice, it seems that often inertia is assumed to be a simple yet irrelevant addition to the balance of forces, for example by Uddin *et al.* (2002) and Phan-Thien, Sugeng & Tanner (1987). The large, relative flatness of the upper surface is what causes the inertia of the particles to become important in our set-up. The geometry used by Uddin *et al.* (2002), for example, used a smaller and more curved sphere, for which we find that $m' \approx 0.0046 m$. (This is found from Uddin's paper by taking $\rho_{\text{sphere}} = 7800 \text{ kg m}^{-3}$ and $R = 20 \text{ mm}$ yielding a sphere mass $m = 26 \text{ g}$. Given that $\rho_{\text{fluid}} = 976 \text{ kg m}^{-3}$ and assuming $Z_{\text{tip}} = 1 \text{ mm}$ and $d = 2 \text{ mm}$ gives $r_m = 62 \text{ mm}$ which thereafter yields $m' = 0.0012 \text{ kg}$.) Therefore, in their case neglecting inertia is perfectly sound. However, the sign and proportionality with acceleration make this term non-trivial to interpret.

At the first moment of impact the fluid particles rapidly accelerate from a standstill to a maximum velocity. At this stage the inertial force is positive, meaning the piston decelerates by transferring its kinetic energy into kinetic energy of the particles. Then, the particles rapidly slow down again to the near standstill of the slow squeezing regime. At this stage the piston is effectively sucked downwards by a negative inertial force, as the kinetic energy of the particles cannot instantly vanish. This kinetic energy can be either be dissipated by viscous forces or escape the gap by fluid escaping at the edges. Intuitively, one might think most of the kinetic energy escapes by fluid moving out of the edges of contact, but in fact, the spherically shaped bottom of the piston allows for a large amount of fluid to remain within the gap, especially near the edges where the gap size is largest. All these fluid particles that remain within the gap will eventually have to return the kinetic energy they initially gained from the falling object, hence yielding a negative force.

From our experimental results in figure 4, we postulate that despite $m' \gg m$ and a large amount of kinetic energy being stored in the fluid, the inertial force plays no role in determining the amount of fluid being squeezed out during the initial stage of impact. The inertia stored in the fluid particles changes rapidly during impact, yet experimental data suggest that this has no net effect on the stopping of the piston. In this view it makes sense that the model including inertia predicts more squeezing than actually experimentally occurs (see the dashed lines in figures 4b,c). The suction of the inertial force is overestimated, as the hydrodynamic description includes the deceleration of the particles starting at $t = 0$, but it does not take into account the initial acceleration.

Furthermore, it is noted that although the term proportional to \dot{h} depends on the distance of the edge of the upper surface, because the particle velocity is highest there. The assumption that pressure returns to ambient pressure at this edge, which is typically used in calculating the inertial force (Jackson 1963; Kuzma 1967; Usha & Vimala 2002), seems

therefore dubious during the moment of impact. Although it is not trivial to define a better alternative for this boundary condition, the condition $p(r = r_m) > 0$ would be able to undo the over-extensive negative force predicted by the model. We also note that suction can only be present if a negative pressure arises underneath the piston, which would result in cavitation. Air would be sucked from the boundaries into the contact and it is complicated to imagine what the precise mathematical implications of such an effect would be.

8. Viscoelastic impact

For both Newtonian and shear-thinning liquids, the data show good agreement with the prediction by fast viscous squeeze theory. This verifies our earlier statement that the viscous force is in fact responsible for slowing down the fast-moving surface to a near standstill, whereas the inertial force plays an insignificant role. However, as the data also show that rapid squeeze out ($h_{start} = 0$) is possible, there is still no explanation for why liquids with similar viscous properties, when tested in a rheometer, can exhibit widely different slipperiness. To explain this, we turn to another liquid property, namely the viscoelasticity.

The relevance of the viscoelastic properties of a liquid during an impact was already discovered by Brindley & Davies (1976) and Binding, Davies & Walters (1976) in 1976, who as a side note found that such a liquid would create a ‘bump’ in the layer thickness vs time curve. Although it is suggested that this bump is responsible for the slipperiness of the liquid, it does not seem to be analysed in depth by others, although others have tried to mathematically capture the phenomena occurring briefly after impact on a viscoelastic liquid (Leider 1974; Leider & Bird 1974; Phan-Thien & Tanner 1984; Phan-Thien *et al.* 1987; Kaushik, Mondal & Chakraborty 2016).

Aqueous solutions of long chain polyethylene oxide have strong viscoelastic properties (Bailey & Koleske 1976; Bird *et al.* 1987) and when put in the piston set-up, we reproduce the bump in the development of the layer thickness from Binding’s work, see figure 5(b). Increasing the polymer concentration enhances the size of this typical viscoelastic bump. The piston moving back up for a short period of time is explained by elasticity generated by the stretching of the individual polymer molecules in the fluid. During the first stage of impact, the fluid squeezes out with high speed and hence high shear, causing the molecules to temporarily store some of the applied energy into elastic energy by means of stretching. Briefly after this first moment of impact, the stretched molecules relax back into their original configuration, creating the process of fluid flowing back into the contact, hence pushing the piston back up during this stage. Only after this phase of stretching and relaxing of the polymers has the system processed the impact and the slow viscous regime will start.

This explanation is further strengthened by the high-speed imaging of the squeezing of a viscoelastic liquid (see figure 5a). For this measurement an additional similar set-up was used to allow for camera capture, as explained in the caption of figure 5. Observed is the initial squeeze out and the elastic recoil occurring within a few milliseconds after impact. The sheet of fluid coming out from underneath the surfaces does not break apart as a Newtonian liquid would do (Sijs & Bonn 2020) but contracts itself partly back towards the gap underneath the piston. The characteristics of the elastic recoil are examined further for several concentrations of PEO 4M and over a range of impact velocities. We define the elastic end time t_e and elastic end layer h_e as respectively the time after impact and the central layer thickness for which the layer thickness is at its maximum, as illustrated in

Impact on a fluid layer

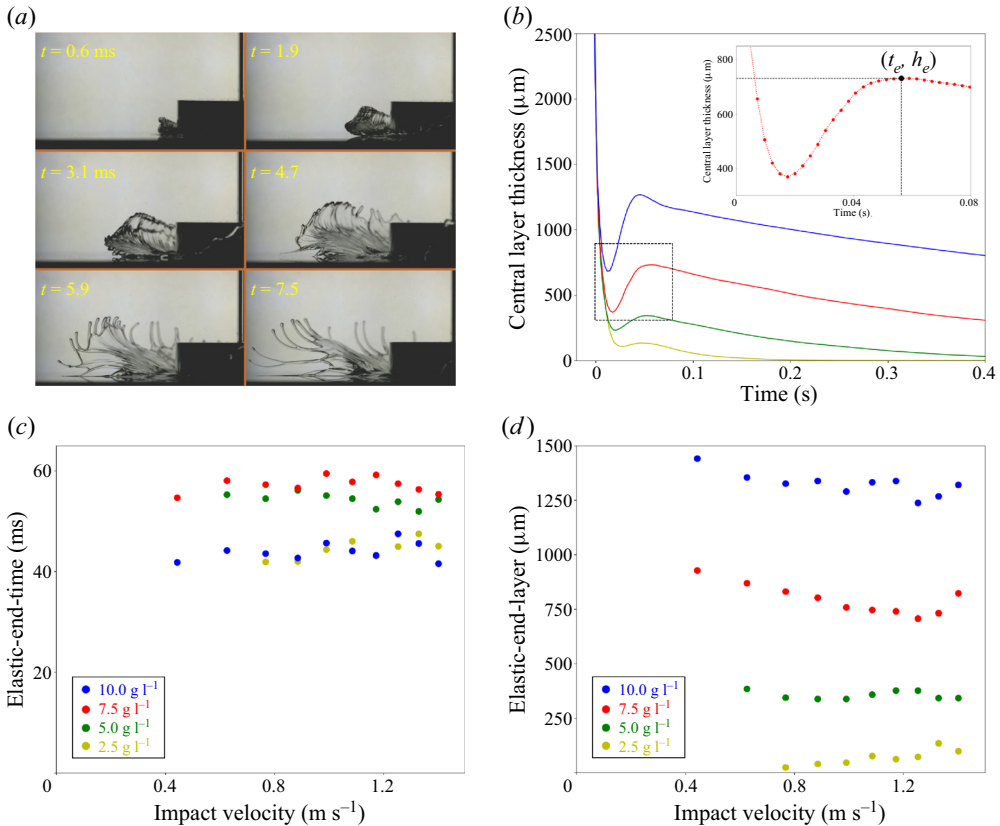


Figure 5. (a) High-speed camera images of the impact of a disk on the highly viscoelastic fluid PEO 4M 10 g l^{-1} . Visible is the elastic response of the liquid. After 4 ms the liquid has a tendency to retract itself back into the contact, as a result of the rapid stretching of the polymer molecules during the first moments of impact. In order to be able to create these images, a slightly different set-up was used. This set-up consisted of a disk with flat bottom, size $r_m = 2 \text{ cm}$ and mass 550 g. It was dropped with velocity 0.4 m s^{-1} onto a fluid layer of thickness 2 mm. (b) The development of central layer thickness during the impact on four different concentrations of PEO 4M. Impact velocity is 1.3 m s^{-1} for all four measurements. As a result of the elasticity, fluid sucks itself back into the gap after impact, pushing the piston back up, resulting in the typical bump in these curves. The inset shows a zoomed-in version of the region in the dotted rectangular box. The dots are data points measured by the induction sensors, which are connected by a dashed line for visual guidance. As shown in the inset, the elastic end time and the elastic end layer are defined as respectively the time and layer thickness at the peak of the bump. (c,d) The elastic end time t_e (c) and the elastic end layer h_e (d) as a function of impact velocity of the piston and polymer concentration. Both t_e and h_e do not depend on impact velocity, which means that a viscoelastic liquid cannot be squeezed out on a short time scale, explaining the slippery properties of these liquids.

the inset of figure 5(b). At this instance the initial elastic impact can be considered finished and the slow viscous regime begins with layer thickness $h_{start} = h_e$.

The elastic end layer depends heavily on the concentration (see figure 5d), which is explained by the large difference in viscosity in the liquids. The impact velocity, however, has little effect on the value of h_e , meaning that one cannot squeeze out a viscoelastic liquid rapidly by increasing this parameter. The elastic end time depends not on impact velocity and only marginally on concentration (see figure 5c). This result is sensible, as the time scale in which the stretching and relaxing takes place is an intrinsic property of the molecule, independent of the precise amount of those molecules in the solution

or the amount of stretching. The elastic end time for the highest (10.0 g l⁻¹) and lowest (2.5 g l⁻¹) concentrations is slightly lower than for the two intermediate concentrations, yet it is unclear whether there is a physical or experimental reason behind this.

From the rheological parameters it is possible to extract a time scale by dividing the first-normal-stress coefficient by viscosity (Bird *et al.* 1987). The precise result of this calculation not only depends on concentration, but is also very sensitive to the way the rheology measurement is performed (de Cagni *et al.* 2019). From our numerical simulation and from the values obtained by dividing impact velocity by initial layer thickness we find a typical shear rate range between 100 and 1000 s⁻¹ for the impacts on the viscoelastic liquids. Within this range time scales of between 10 and 50 ms are found for the PEO 4M concentrations (see figure 6a). This time scale has the same order of magnitude as the elastic end time, so likely these quantities are closely linked to each other. This idea is supported by the results for the two mostly inelastic fluids PEO 2M and Xanthan Gum, which have a time scale roughly an order of magnitude lower at the higher end of the shear rate range. This explains why these fluids do not show any viscoelastic behaviour during impact, whilst they do exhibit (small) normal stresses in the rheology measurements. In fact, the concentration of PEO 2M 10.0 g l⁻¹ actually yields a higher normal stress than the PEO 4M 2.5 g l⁻¹, see figure 1(f,g), but because the former has smaller molecules its relaxation time is much shorter no characteristic bump is found in the impact experiment.

As a result of t_e and h_e both being constant with respect to impact velocity within the range of parameters tested here, it can be concluded that, for every piston impact, the slow viscous regime starts at the same layer thickness at the same time after impact. It is therefore impossible to completely drain a viscoelastic liquid on a short time scale \bar{t} . This explains the slipperiness of the PEO 4M solutions discussed in the introduction, since the gap between foot and surface is lubricated for a relatively long time during the slow viscous regime, giving e.g. the foot or shoe no grip on the surface, resulting in the victim falling. In contrast to stepping on a non-viscoelastic liquid, the kinetic energy the victim provides during his step plays no role, as it will counterintuitively not change the amount of fluid left underneath his foot, as showed by the experiments.

The impact on a viscoelastic fluid can be modelled by a Jeffreys model, which is an often used constitutive equation that adds elasticity to a Newtonian liquid (Bird *et al.* 1987)

$$\boldsymbol{\tau} + \lambda_1 \frac{\partial \boldsymbol{\tau}}{\partial t} = -\eta_0 \left(\dot{\boldsymbol{\gamma}} + \lambda_2 \frac{\partial \dot{\boldsymbol{\gamma}}}{\partial t} \right). \quad (8.1)$$

Here, the shear stress $\boldsymbol{\tau}$ does not solely depend on the present shear rate $\dot{\boldsymbol{\gamma}}$, but also on its past development, as may be apparent by the time dependency in (8.1). The model included three parameters: the Newtonian viscosity η_0 , the relaxation time of the polymer λ_1 and the retardation time of the polymer λ_2 . Many of those types of fluid models exist, and any choice has advantages and disadvantages. We have chosen the Jeffreys model for its relative simplicity, yet still being capable of reproducing the experimentally observed effects. An obvious disadvantage of this model is its Newtonian behaviour in the absence of any elastic effects, whereas the liquids tested all exhibit clear shear-thinning properties.

In Appendix D it is worked out that a workable formula for the viscoelastic force the fluid applies on the piston is given by the well-known Newtonian viscous force (Maude 1961) compensated by a memory function that contains information about the

Impact on a fluid layer

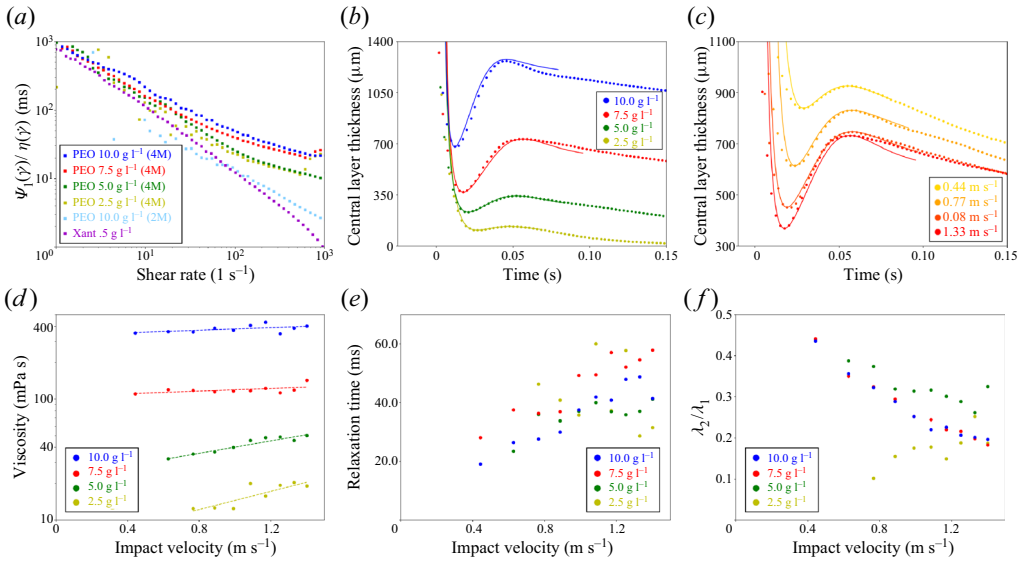


Figure 6. (a) The time scale that can be derived from rheological data by dividing the first-normal-stress coefficient by the viscosity for all six shear-thinning fluids. (b) Development of the central layer thickness as a function of time for three concentrations of PEO 4M impacted by the piston with velocity 1.33 m s^{-1} (data points). The lines display the fits using the Jeffreys model. As the Jeffreys model does not describe shear thinning, it makes no sense to use it for the slow viscous regime, so the curves terminate after a time $2t_e$. (c) The development of the central layer thickness for PEO 7.5 g l^{-1} with four different impact velocities. (d–f) Respectively the values of η_0 , λ_1 and the ratio λ_2/λ_1 that are found by the fitting process as a function of impact velocity. The dashed line in (d) displays the slightly upwards trends in the viscosity results. For the three highest concentrations of PEO (4M), the ratio in (f) grows towards 1 when lowering the impact velocity, indicating that viscoelastic effects are less prominent at low piston speed. The fitting results for the retardation time λ_2 can be found in figure 8 in Appendix D.

fluid movement in the past

$$F_{ve} = \frac{-6\pi\eta_0 R^2 \dot{h}(t)}{h_0(t)} \frac{s_m^4}{(1 + s_m^2)^2} M(t, t'), \quad (8.2)$$

with the memory function $M(t, t')$ defined in the following way:

$$M(t, t') = \left(1 - \frac{\lambda_2}{\lambda_1}\right) \frac{h_0(t)^2}{\lambda_1 \dot{h}(t)} \int_{t'=-\infty}^{t'=t} \frac{\dot{h}(t')}{h_0(t')^2} e^{-(t-t')/\lambda_1} dt' + \frac{\lambda_2}{\lambda_1}. \quad (8.3)$$

The derivation of these formulas relies on an assumption that has not been fully proven mathematically, but we will show here that (8.2) works well as a model to capture the underlying physics for an impact on a viscoelastic fluid. For as long as layer thickness changes significantly within a time scale λ_1 , elastic effects have influence, and otherwise the memory function becomes equal to 1 and the result for ordinary Newtonian squeeze flow remains in (8.2).

The development of the central layer thickness as a result of the viscoelastic force is simulated for modelling the first milliseconds after impact by applying a forward Euler algorithm on the equation of motion given by (3.4). The experimental values $h_0(t=0) = X_0$ and $\dot{h}(t=0) = -v_0$ are used as the initial condition for the simulation and the three parameters η_0 , λ_1 and λ_2 are considered fitting parameters that are optimized to match

model and data. The \dot{h}^2 term of the inertia according to (3.3) was included, but the ‘virtual mass’ term was excluded, since we argue it is unphysical.

The usage of the viscoelastic force given by (8.2) yields a bump in the layer thickness profile that is similarly shaped to the experimental results. The fitting of the parameters η_0 , λ_1 and λ_2 on the experimental data was performed by minimizing the difference between experimental data and simulation for these three characteristics: the lowest point in the bump, the highest point in the bump and the time difference between these points. We do not constrain ourselves in allowing only one set of parameters (η_0 , λ_1 , λ_2) per fluid, but rather we fit the parameters for each individual impact measurement and interpret the obtained parameters. The viscoelastic effects of the fluid are expected to play no role anymore during the slow viscous regime (Binding *et al.* 1976; Engmann *et al.* 2005), so for $t > 2t_e$ the simulation ends. The precise moment at which to stop the simulation is somewhat arbitrary, yet it has to be done somewhere, as the Jeffreys model is incapable of capturing the shear-thinning behaviour of the slow viscous decay. The simulation can reproduce the impact on the different concentrations of PEO (4M) for different impact velocities (see figure 6*b,c*).

Just like the viscosity found by the rheometer, the fitted viscosity grows on increasing the polymer concentration, see figure 6*(d)*; the scaling is similar. The impact velocity has little influence on the fitted viscosity, which is remarkable as it could be expected that the shear-thinning properties would cause the fluid to be thinner at higher impact. The results suggest that during the short time scale in which elastic stresses dominate the shear thinning becomes irrelevant. The results for the lower polymer concentrations, 2.5 g l^{-1} and 5.0 g l^{-1} , even seem to suggest that the liquid gets thicker for higher impact velocity. However, that the viscoelastic properties during impact are comparable to a shear-thickening effect is something that has been found before (de Goede *et al.* 2019).

The fitted values for the relaxation time λ_1 fall within a range between 20 and 60 ms, similar to the elastic end time, see figure 6*(e)*. This time scale is thus also in the same range as the elastic end time t_e and the viscoelastic time scale inferred from the rheological data. Therefore, the rheology data might intrinsically contain an estimate for which relaxation time to use in the Jeffreys model. However, the dependence of these parameters on velocity is different for all three: the fitted relaxation time increases with velocity, the elastic end time is constant and the time scale extracted from the rheological data decreases with velocity.

The ratio between retardation time and relaxation time is expected to be between 0 and 1, with 0 resulting in the simpler Maxwell model and with 1 resulting in the complete absence of viscoelastic stresses (Bird *et al.* 1987). Simulations with the Maxwell model have been tried and they cause the model to behave too elastic, as the predicted oscillation of the piston continues for too long, so that more than one bump is predicted. The inclusion of the retardation time dampens these oscillations. At an impact velocity above 0.8 m s^{-1} the ratio is found to be 0.25 ± 0.10 , see figure 6*(f)*. At low impact velocity it is expected that viscoelasticity plays a lesser role, due to the lesser amount of stress imposed on the liquid. This is observed in the trend for the ratio λ_2/λ_1 . It grows closer towards 1 when lowering impact velocity, which we interpret as the viscoelastic effects becoming less prominent for these types of impact. (In this limit the Jeffreys model would turn into the simple case of a Newtonian fluid.) It remains unclear to the authors why the concentration 2.5 g l^{-1} displays the opposite trend, although it is noted that a relatively low layer thickness, in some cases close to zero, for this fluid leads to quite extreme simulation conditions, and the convergence of the fit is poorer than for the other concentrations.

With these results, it might be possible to suggest a way to roughly predict the squeeze flow of a viscoelastic liquid from only its rheological data. Firstly, an average shear rate during the squeezing has to be estimated. Then, a characteristic time scale λ_1 for the viscoelastic regime can be extracted from the ratio between the first-normal-stress coefficient and viscosity at that given shear rate. This time scale serves as the relaxation time in the Jeffreys model. To complete the model, the viscosity η_0 can be taken from the flow curve at the average shear rate and the retardation time λ_2 can be assumed to be roughly a factor 4 smaller than λ_1 . Then, (8.2) is capable of predicting the viscoelastic regime of the impact during the time scale $2\lambda_1$, after which slow viscous shear-thinning squeeze described by (3.1) follows until all the fluid is squeezed out of the gap. Although this method is very crude and more experimental evidence is required to verify its correctness, it seems plausible that the relatively simple rheometer measurement contains all information necessary to precisely predict the more complicated fluid behaviour under high velocity impact.

9. Conclusion

In conclusion, it is found that the slipperiness of certain fluids can be explained by their response on high velocity impact. During the first stage of the squeezing process a part of the initial fluid layer drains rapidly and the amount of fluid remaining within the gap is determined by the viscous dissipation of the kinetic energy of the piston. If the impact velocity is high enough, practically all of the fluid can be squeezed out within this short time scale and the lubricating layer will not exist long enough to give the fluid a slippery sensation. However, for impact on viscoelastic polymeric solutions, a part of the kinetic energy is temporarily stored as elastic energy within the stretched molecules in the fluid. The elastic recoil of these molecules causes fluid to be sucked back into the contact, making these types of liquids particularly resistant to rapid drainage and explaining their slippery nature.

Funding. This research was performed within the framework of the ‘Molecular aspects of biopolymers defining food texture perception and oral digestion’ project funded by NWO (The Netherlands Organization for Scientific Research), grant number 731.017.201, Unilever and Anton Paar.

Declaration of interest. The authors report no conflict of interest.

Author ORCIDs.

 D. Bonn <https://orcid.org/0000-0001-8925-1997>.

Appendix A. Derivation of the viscous squeezing force

Squeezing a fluid yields an upwards force. To derive this force, the flow profile of the fluid within the contact needs to be calculated. The derivation of the force coming from the viscosity term of the Navier–Stokes equations is a quite standard procedure (Maude 1961; Cox & Brenner 1967; Engmann *et al.* 2005). For the particular case of a power-law liquid being squeezed by a sphere, the solution has been found by Rodin (1996) and later by Lian *et al.* (2001). In this appendix we will closely stick to the analysis of Lian, but we deviate when we do not place the boundary infinitely far away. The inertial part of the Navier–Stokes equations is trickier to include, and therefore this will be worked out in [Appendix B](#) instead.

To derive the viscous force (and later also the inertial force) the flow profile is retrieved within the gap between surface and piston depicted in [figure 1\(c\)](#). The following definition

of dimensionless coordinates and parameters will prove useful later:

$$\tilde{z} \equiv \frac{z}{h}, \tag{A1}$$

$$s \equiv \frac{r}{\sqrt{2Rh_0}}. \tag{A2}$$

The gap size simplifies in these coordinates to

$$h = h_0 + \frac{r^2}{2R} = h_0(1 + s^2), \tag{A3}$$

and the boundary of pistons surface located at $r = r_m$ is in dimensionless coordinates located at

$$s_m \equiv \frac{r_m}{\sqrt{2Rh_0}}. \tag{A4}$$

As is typical for squeeze flow calculations (Engmann *et al.* 2005), we continue by assuming that the gap size $h(r)$ is very small compared with the characteristic horizontal distance r_m . Therefore, the dominant terms in the \hat{r} -projection of the Navier–Stokes equations determine the flow profile. In the defined dimensionless coordinates and by using the power-law viscosity model (Bird *et al.* 1987), this equation reads

$$\frac{\partial p}{\partial r} = \frac{K}{h(r)^{1+n}} \frac{\partial}{\partial \tilde{z}} \left(\frac{\partial u_r}{\partial \tilde{z}} \right)^n. \tag{A5}$$

As normal in the lubrication approximation, it can be assumed that pressure does not depend on \tilde{z} as a first-order approximation (Maude 1961; Engmann *et al.* 2005). Therefore, the velocity profile $u_r(r, \tilde{z})$ is solved by integrating twice. Using a no-slip boundary condition on both the upper and lower surfaces solves the integration constants, yielding

$$u_r(r, \tilde{z}) = \left(-\frac{\partial p}{\partial r} \frac{h(r)}{K} \right)^{1/n} \frac{h(r)}{1 + \frac{1}{n}} \left(\left(\frac{1}{2} \right)^{1/(n+1)} - \left| \frac{1}{2} - \tilde{z} \right|^{1/(n+1)} \right). \tag{A6}$$

Next, the pressure profile is solved by imposing the incompressibility constraint. This implies that the volume of fluid being squeezed out of the gap must be equal to the volume of fluid being expelled by the lowering of the upper surface

$$2\pi r \int_0^{h(r)} u_r \, dz = -\pi r^2 \dot{h}. \tag{A7}$$

The integral is performed, and solving the resulting equation for the pressure term yields

$$\frac{\partial p}{\partial r} = -2 \left(2 + \frac{1}{n} \right)^n K (-\dot{h})^n \frac{r^n}{h(r)^{2n+1}}. \tag{A8}$$

To continue from here, a transition into dimensionless coordinates as defined in (A1) and (A2) is used. At the boundary $s = s_m$, the pressure must return to ambient

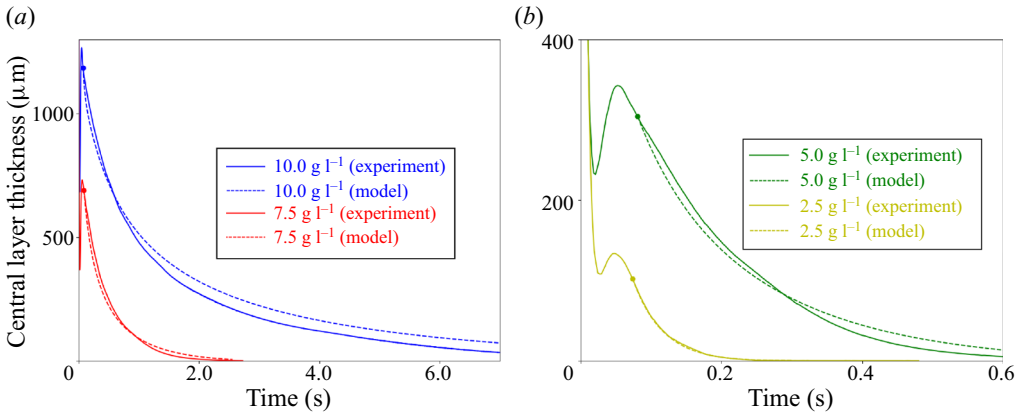


Figure 7. The development of layer thickness during the slow viscous squeeze of the viscoelastic liquid PEO 4M with concentrations 10.0 g l^{-1} , 7.5 g l^{-1} (a) and 5.0 g l^{-1} , 2.5 g l^{-1} (b). The curves are modelled by (A14) with the dots in the figures corresponding to the starting conditions that are used. The agreement between model and experiment confirms the idea that viscoelastic forces play no role in the slow viscous regime.

pressure, which is defined as zero here, so that the positional integral of (A8) then gives a solution for the pressure

$$p = 2 \left(2 + \frac{1}{n} \right)^n K(-\dot{h})^n \frac{(2Rh_0)^{1/2+(1/2)n}}{h_0^{2n+1}} \int_{s_m}^s \frac{s^n}{(1+s^2)^{2n+1}} ds. \quad (\text{A9})$$

Finally, the viscous force on the piston is given by the integral of the pressure over the entire surface of the piston. The integral is calculated using the dimensionless coordinates

$$F_v = 2\pi \int_0^{r_m} p(r)r dr = 4\pi Rh_0 \int_0^{s_m} p(s)s ds. \quad (\text{A10})$$

The viscous force is thus given by

$$F_v = \frac{K(-\dot{h})^n R^{3/2+(1/2)n}}{h_0^{(3/2)n-1/2}} X(s_m), \quad (\text{A11})$$

with the function $X(s_m)$ being defined as

$$X(s_m) = 8 \left(2 + \frac{1}{n} \right)^n 2^{(1+n)/2} \pi \int_0^{s_m} \int_{s_m}^{s'} \left(\frac{s^n}{(1+s^2)^{2n+1}} \right) s' ds'. \quad (\text{A12})$$

The inner integral in (A12) can only be solved in closed form for specific values of n . For $n = 1$ all integral can be performed and the viscous force returns to the well-known formula for the squeeze of a Newtonian liquid underneath a spherical piston (Maude 1961; Cox & Brenner 1967)

$$F_v^{n=1} = -\frac{6\pi\eta R^2 \dot{h}}{h_0}. \quad (\text{A13})$$

For the calculations displayed in the main manuscript, the function $X(s_m)$ was calculated numerically and tabulated for several values of n , which allowed for quick usage. As described in the main text, an exact expression for the development of the layer thickness

during slow viscous squeezing can be found in the literature for the Newtonian case (Maude 1961). For more general values of n , the equation of movement

$$m\ddot{h} = F_v, \tag{A14}$$

with F_v given by (A11) was solved numerically. This was done by starting with the initial conditions $h_0(t = 0) = h_{start}$ and $\dot{h}(t = 0) = -v_{start}$ and using the forward Euler method on (A14). For the slow viscous regime this method gives a prediction in agreement with our experimental findings for both PEO 2M (see figure 2c) and all samples of the more viscoelastic PEO 4M (see figure 7). Note that the values K and n are retrieved from the flow curves of the rheometer measurement, so that no fitting parameters are used in the creation of these curves.

Appendix B. Derivation of the inertial squeezing force

The fluid velocity profile within the gap is harder to find if one includes the inertial terms of the Navier–Stokes equations. Here, we will follow the procedure established by Jackson (1963) and improved by Kuzma (1967), which gives a good estimation for the inertial term. The method was developed for a flat–flat geometry, but a similar derivation for a flat–sphere geometry can be provided following the same steps. The procedure consists of taking a universal velocity profile \bar{u}_r and \bar{u}_z independent of z , which is substituted into the inertial part of the Navier–Stokes equations. Then, from the viscous term in the Navier–Stokes equations an updated version of the velocity profile is found, which is used to obtain the formulas for pressure and force on the upper surface. Ideally, the updated velocity profile should be substituted back into the inertial part of the Navier–Stokes equations iteratively, leading to a converging scheme for the velocity profile. However, because Kuzma found that only this single iteration already provides a reasonable approximation of the inertial force, we limit ourselves to only substituting the initial universal velocity profile and directly calculating the resulting pressure profile thereafter. The inertial part of the \hat{r} -projection of Navier–Stokes reads

$$\rho \left(\frac{\partial \bar{u}_r}{\partial t} + \bar{u}_r \frac{\partial \bar{u}_r}{\partial r} + \bar{u}_z \frac{\partial \bar{u}_r}{\partial z} \right) = -\frac{\partial p}{\partial r}. \tag{B1}$$

According to the procedure, \bar{u}_r and \bar{u}_z have been substituted into the left-hand side of (B1). The term $\partial \bar{u}_r / \partial z$ is not included by Jackson (1963), because \bar{u}_r does not depend on z in his analysis. However, Kuzma (1967) performed a more thorough analysis including the dependence on z and found that the term $\bar{u}_z(\partial \bar{u}_r / \partial z)$ contributes equally much to the pressure as the term $\bar{u}_r(\partial \bar{u}_r / \partial r)$. Because we are here dealing with a spherical upper surface, the dependence of u_z on z is non-trivial to obtain, so precisely repeating Kuzma’s steps is non-trivial too. However, we will assume that a small curvature of the upper surface does not change the observation about the term $\bar{u}_z(\partial \bar{u}_r / \partial z)$, so that we can circumvent the problems with the third term in the left-hand side of (B1) by putting it equal to the term $\bar{u}_r(\partial \bar{u}_r / \partial r)$

$$\rho \left(\frac{\partial \bar{u}_r}{\partial t} + 2\bar{u}_r \frac{\partial \bar{u}_r}{\partial r} \right) = -\frac{\partial p}{\partial r}. \tag{B2}$$

From here, we can continue using the same steps Jackson uses. The average velocity in \hat{r} -direction is given by

$$\bar{u}_r = -\frac{\dot{h}r}{2h}. \tag{B3}$$

Note that this expression is obtained directly from the incompressibility constraint (see (A7)), and it is therefore equally valid for both Newtonian and non-Newtonian liquids. If the iterative procedure were to be continued for more than one step, the value of n would become important, as $n = 1$ would yield the ordinary parabolic fluid profile on the second iteration, whereas $n < 1$ would not. Because only a single step of the iterative procedure is used here, the result will not depend on the value of n . For our analysis, a higher amount of precision including the dependence on n is not necessary.

Whilst taking into account that \dot{h} depends on time, and h depends on both time and position, (B3) is substituted into (B2), yielding

$$-\frac{\partial p}{\partial r} = \rho \left(-\frac{\ddot{h}r}{2h} + \frac{\dot{h}^2 r}{h^2} - \frac{\dot{h}^2 r^2}{2h^3} \frac{\partial h}{\partial r} \right). \tag{B4}$$

The analysis differs here from Jackson (1963) and Kuzma (1967), because the curved surface is taken into account now. The parabolic gap profile yields $\partial h/\partial r = r/R$, after which the positional coordinate r is swapped by its dimensionless counterpart s using (A1) and (A2), yielding

$$\frac{\partial p}{\partial s} = \rho R \ddot{h} \frac{s}{1+s^2} - 2\rho R \frac{\dot{h}^2}{h_0} \frac{s}{(1+s^2)^3}. \tag{B5}$$

Identically to the calculation of the viscous force, at the boundary $s = s_m$ the pressure is assumed to return to ambient pressure, which is defined as zero here. For the two terms in (B5) the integral can be performed, which results in

$$p = \frac{1}{2} \rho R \ddot{h} \log \left(\frac{s^2 + 1}{s_m^2 + 1} \right) + \frac{1}{2} \rho R \frac{\dot{h}^2}{h_0} \left(\frac{1}{(1+s^2)^2} - \frac{1}{(1+s_m^2)^2} \right). \tag{B6}$$

Next, the inertial force is found by integrating the pressure over the surface of the piston, identically to (A10):

$$F_i = -\pi \rho R^2 \ddot{h} h_0 (s_m^2 - \log(1+s_m^2)) + \pi \rho \dot{h}^2 R^2 \frac{s_m^4}{(1+s_m^2)^2}. \tag{B7}$$

Just as for Jackson (1963) and Kuzma (1967), the inertial force consists of a part that depends on acceleration \ddot{h} and a part that resembles a Bernoulli-like force that depends on the velocity squared \dot{h}^2 . Finally, (B7) can be simplified further if the boundary is assumed to be infinitely far away. For $s_m \rightarrow \infty$ the s_m^2 term dominates the acceleration term, and the boundary factor in the \dot{h}^2 term becomes 1. By substituting s_m using (A4), it is found that

$$F_i \approx -\frac{1}{2} \pi \rho r_m^2 R \ddot{h} + \pi \rho R \dot{h}^2. \tag{B8}$$

This formula gives an approximation for the force due to fluid inertia underneath the piston. Using more than one iteration of the procedure described by Jackson only updates the factors in front of the terms in (B8) to a better approximation. However, for Jackson the next iteration only improves these factors by 20% and there appears to be no reason to believe that for a flat-sphere geometry the improvement by an extra iteration would be significantly different. For the usage in this manuscript, (B8) is therefore sufficiently accurate.

Appendix C. Solving the fast viscous characteristic differential equation

The characteristic differential equation for fast viscous squeezing is given by

$$m\ddot{h} = F_v. \tag{C1}$$

Using the viscous force given in (A11), this equation can be rewritten into

$$\ddot{h}h_0^{(3/2)n-1/2} = (-\dot{h})^n \frac{KR^{3/2+(1/2)n}X(s_m)}{m}. \tag{C2}$$

Given the initial layer thickness X_0 and impact velocity v_0 , the following dimensionless parameters are introduced:

$$\tilde{h} \equiv \dot{h} \frac{X_0}{v_0^2}, \tag{C3}$$

$$\tilde{h} \equiv \frac{\dot{h}}{v_0}, \tag{C4}$$

$$\tilde{h}_0 \equiv \frac{h_0}{X_0}, \tag{C5}$$

$$\tilde{t} \equiv t \frac{v_0}{X_0}, \tag{C6}$$

$$f \equiv \frac{KR^{3/2+(1/2)n}X(s_m \rightarrow \infty)X_0^{3/2-(1/2)n}}{mv_0^{2-n}}. \tag{C7}$$

Which turns (C2) into

$$\tilde{h}\tilde{h}_0^{(3/2)n-1/2} = (-\tilde{h})^n \frac{X(s_m)}{X(s_m \rightarrow \infty)}f. \tag{C8}$$

This equation has to be solved for $\tilde{h}_0(\tilde{t})$ given the initial conditions

$$\tilde{h}_0(\tilde{t} = 0) = 1, \tag{C9}$$

$$\tilde{h}(\tilde{t} = 0) = -1. \tag{C10}$$

Even for the specific case $n = 1$ and $s_m \rightarrow \infty$, a closed form solution of (C8) does not exist (Polyanin & Zaitsev 2003). Therefore, it must be solved by numerical means. With the use of a forward Euler algorithm the development of $\tilde{h}_0(\tilde{t})$ has been retrieved. A few examples of this process are shown in figure 3(b) in the main text. It is observed that (C8) reaches a stable value of $\tilde{h}_0(\tilde{t})$ for $\tilde{t} \gg 1$, for which the precise value depends on f . Hence, the fraction of the initial layer left is a function of the parameter f . By running the algorithm over different values of n and f this relation is found, the result of which is shown in figure 4(a) in the main text. In the creation of figure 4(a) the assumption $s_m = 0.92$ was used at $\tilde{t} = 0$, according to our experimental conditions. Thereafter, for $\tilde{t} > 0$, s_m was calculated each iteration by using the property that it scales with $\tilde{h}_0^{-1/2}$.

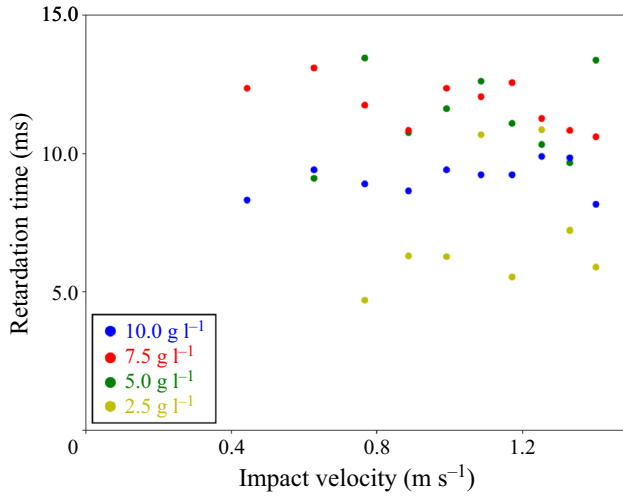


Figure 8. The fitted retardation time λ_2 for impact measurements as a function of impact velocity with four different concentrations of PEO (4M). The fitting results for the viscosity η_0 and relaxation time λ_1 can be found in respectively figures 6(d) and 6(e) in the main text.

Appendix D. Derivation of the viscoelastic force by implementation of the Jeffreys model

The Jeffreys model leads to a consecutive relation given by Bird *et al.* (1987),

$$\tau = - \left(1 - \frac{\lambda_2}{\lambda_1} \right) \int_{t'=-\infty}^{t'=t} \frac{\eta_0}{\lambda_1} e^{-(t-t')/\lambda_1} \dot{\gamma}(t') dt' - \eta_0 \frac{\lambda_2}{\lambda_1} \dot{\gamma}(t). \quad (D1)$$

Even though the current shear stress now depends on the shear rate $\dot{\gamma}(t')$ of the past, the derivation of the force on the piston follows the same steps as the one for Newtonian squeezing. The flow profile reads

$$u_r(r, \tilde{z}) = -3\dot{h} \frac{r}{h(r)} \tilde{z}(1 - \tilde{z}). \quad (D2)$$

It must be noted that the dimensional part of this result is directly obtained from the incompressibility constraint (A7) and not necessarily from the Navier–Stokes equations, and hence (D2) works equally well for the implementation of the Jeffreys model. The parabolic dependency on \tilde{z} is a consequence of the Navier–Stokes equations, but because the no-slip boundary conditions remain applicable, it is reasonable to assume the Jeffreys model implementation does not affect the dependency of u_r on \tilde{z} .

The dominant element of $\dot{\gamma}$ to be used in the lubrication approximation is $\dot{\gamma}_{rz}$. Using (D2) it is found that

$$\dot{\gamma}_{rz} = \frac{\partial u_r}{\partial z} = -3\dot{h} \frac{r}{h(r)^2} (1 - 2\tilde{z}). \quad (D3)$$

Using this expression, it follows from (D1) that the shear stress on the top surface at $\tilde{z} = 1$ is given by

$$\tau_{rz} = 3 \left(1 - \frac{\lambda_2}{\lambda_1} \right) \frac{\eta_0}{\lambda_1} r \int_{t'=-\infty}^{t'=t} \frac{\dot{h}(t')}{h(r, t')^2} e^{-(t-t')/\lambda_1} dt' + 3 \frac{\lambda_2}{\lambda_1} \eta_0 \dot{h} \frac{r}{h(r)^2}. \quad (D4)$$

Substituting the dimensionless s -coordinate in the place of r yields

$$\begin{aligned} \tau_{rz} = & 3 \left(1 - \frac{\lambda_2}{\lambda_1} \right) \frac{\eta_0}{\lambda_1} \sqrt{2Rh_0s} \int_{t'=-\infty}^{t'=t} \frac{\dot{h}(t')}{h_0(t')^2(1+s^2)^2} e^{-(t-t')/\lambda_1} dt' \\ & + 3\sqrt{2}\eta_0 \frac{\lambda_2}{\lambda_1} \frac{\dot{h}}{h_0} \sqrt{\frac{R}{h_0}} \frac{s}{(1+s^2)^2}. \end{aligned} \quad (D5)$$

The proximity of the boundary s_m depends on the central layer thickness $h_0(t)$ and hence the coordinate system using s as special coordinate depends on time. Therefore, the factor $1/(1+s^2)^2$ can technically not be taken outside the integral for as long as s_m has changed significantly during the past time λ_1 . For computational purposes it is now falsely assumed that s can in fact be taken outside the integral, and upon finding the final result of this derivation, we will discuss the consequences of this decision. The stress can now be written as

$$\tau_{rz} = 3\sqrt{2}\eta_0 \frac{\dot{h}}{h_0} \sqrt{\frac{R}{h_0}} \frac{s}{(1+s^2)^2} M(t, t'), \quad (D6)$$

with $M(t, t')$ a memory function and the factor in front of it identical to the shear stress for Newtonian squeeze flow

$$M(t, t') = \left(1 - \frac{\lambda_2}{\lambda_1} \right) \frac{h_0(t)^2}{\lambda_1 \dot{h}(t)} \int_{t'=-\infty}^{t'=t} \frac{\dot{h}(t')}{h_0(t')^2} e^{-(t-t')/\lambda_1} dt' + \frac{\lambda_2}{\lambda_1}. \quad (D7)$$

From here on, the derivation is identical to that of Newtonian squeeze, with the memory function carried along in each step. Since the memory function contains no coordinate parameters, any integrals over position are unaffected by it. We continue by deriving the pressure distribution with the lubrication approximation $\partial p/\partial r = \partial \tau_{rz}/\partial z$, after which the pressure is integrated over the surface of the upper surface to find the total force, yielding the Newtonian viscous force multiplied by the memory function

$$F = -\frac{6\pi\eta_0 R^2 \dot{h}(t)}{h_0(t)} \frac{s_m^4}{(1+s_m^2)^2} M(t, t'). \quad (D8)$$

As mentioned before, this result is obtained by neglecting the dependence of the memory function on position. The term $s_m^4/(1+s_m^2)^2$ is obtained by two separate integrals over s that were only possibly under the assumption that the factor $1/(1+s^2)^2$ in (D5) can be taken in front of the integral sign. A mathematically better approach would consist of including position in the memory function as well, and integrating over both time and position to obtain the viscoelastic force at a given instance. However, this procedure would be computationally more advanced up to the point that it would provide little extra practical benefit over the thorough analyses of for example Phan-Thien *et al.* (1987) and Kaushik *et al.* (2016). There is, however, a mathematical trick that allows us to verify that (D8) is a reasonable estimate of the real force predicted by the Jeffreys model. Instead of taking all s outside the memory integral, as explained between (D5) and (D6), we can also take all s inside the integral, which would result in the proximity of the boundary term $s_m^4/(1+s_m^2)^2$

being excluded in (D8) and instead included in the memory function as

$$\tilde{M}(t, t') = \left(1 - \frac{\lambda_2}{\lambda_1}\right) \frac{h_0(t)^2}{\lambda_1 \dot{h}(t)} \int_{t'=-\infty}^{t'=t} \frac{\dot{h}(t')}{h_0(t')^2} \frac{s_m(t')^4}{(1 + s_m(t')^2)^2} e^{-(t-t')/\lambda_1} dt' + \frac{\lambda_2}{\lambda_1} \frac{s_m^4}{(1 + s_m^2)^2}, \quad (\text{D9})$$

$$\tilde{F} = -\frac{6\pi\eta_0 R^2 \dot{h}(t)}{h_0(t)} \tilde{M}(t, t'). \quad (\text{D10})$$

This would mathematically be an equally false approach as the one used before, but because (D8) and (D10) denote the two extreme cases (namely, taking either all s inside or all s outside the integral) of calculating the force, the real force predicted by the Jeffreys model will be in between. We tested both formulas for fitting our experimental data, and we found that both models can replicate the typical viscoelastic bump and that the fitting parameters η_0 , λ_1 and λ_2 have the same order of magnitude in both cases. Therefore, we conclude that the choice of taking $1/(1 + s^2)^2$ outside of the integral in (D5) has little influence the simulations and that the oversimplified force given in (D8) is actually a good and practical approximation for the range of parameters tested in this manuscript. We used (D8) rather than (D10) to obtain the simulation results discussed in the main text, as intuitively it makes sense that the force should be proportional to the piston surface area πr_m^2 at any given instance.

REFERENCES

- ADAMS, M.J., EDMONDSON, B., CAUGHEY, D.G. & YAHYA, R. 1994 An experimental and theoretical study of the squeeze-film deformation and flow of elastoplastic fluids. *J. Non-Newtonian Fluid Mech.* **51**, 61–78.
- AKERS, B. & BELMONTE, A. 2006 Impact dynamics of a solid sphere falling into a viscoelastic micellar fluid. *J. Non-Newtonian Fluid Mech.* **108**, 133–146.
- ARDEKANI, A.M., JOSEPH, D.D., DUNN-RANKIN, D. & RANGEL, R.H. 2009 Particle-wall collision in a viscoelastic fluid. *J. Fluid Mech.* **633**, 475–483.
- BAILEY, F.E. & KOLESKE, J.V. 1976 *Poly(Ethylene Oxide)*. Academic Press.
- BINDING, D.M., DAVIES, J.M. & WALTERS, K. 1976 Elastico-viscous squeeze films part 2: superimposed rotation. *J. Non-Newtonian Fluid Mech.* **1**, 259–275.
- BIRD, R.B., ARMSTRONG, R.C. & HASSAGER, O. 1987 *Dynamics of Polymeric Liquids, Volume 1: Fluid Mechanics*, 2nd edn. Wiley.
- BRINDLEY, G. & DAVIES, J.M. 1976 Elastico-viscous squeeze films part 1. *J. Non-Newtonian Fluid Mech.* **1**, 19–37.
- BRUUS, H. 2008 *Theoretical Microfluidics*. Oxford University Press.
- DE CAGNI, H., FAZILATI, M., HABIBI, M., DENN, M.M. & BONN, D. 2019 The yield normal stress. *J. Rheol.* **63**, 285.
- CAMPANELLA, O.H. & PELEG, M. 2002 Squeezing flow viscometry for nonelastic semiliquid foods - theory and applications. *Crit. Rev. Food Sci. Nutr.* **42** (3), 241–264.
- COX, R.G. & BRENNER, H. 1967 The slow motion of a sphere through a viscous fluid towards a plane surface – II small gap widths, including inertial effects. *Chem. Engng Sci.* **22**, 1753–1777.
- DEBLAIS, A., DEN HOLLANDER, E., BOUCON, C., BLOK, A.E., VELTKAMP, B., VOUDOURIS, P., VERSLUIS, P., KIM, H., MELLEMA, M. & STIEGER, M. 2021 Predicting thickness perception of liquid food products from their non-Newtonian rheology. *Nat. Commun.* **12** (1), 6328.
- ENGMANN, J., SERVAIS, C. & BURBIDGE, A.S. 2005 Squeeze flow theory and applications to rheometry: a review. *J. Non-Newtonian Fluid Mech.* **132**, 1–27.
- DE GOEDE, T.C., DE BRUIN, K.G. & BONN, D. 2019 High-velocity impact of solid objects on non-Newtonian fluids. *Sci. Rep.* **9**, 1250.
- GRIMM, R.J. 1976 Squeezing flows of Newtonian liquid films. An analysis including fluid inertia. *Appl. Sci. Res.* **32**, 149–166.
- HAMROCK, B.J., SCHMID, S.R. & JACOBSON, B.O. 2004 *Fundamentals of Fluid Film Lubrication*. CRC Press.

- ISHIZAKA, K., LEWIS, S.R. & LEWIS, R. 2017 The low adhesion problem due to leaf contamination in the wheel/rail contact: bonding and low adhesion mechanisms. *Wear* **378**, 183–197.
- JACKSON, J.D. 1963 A study of squeezing flow. *Appl. Sci. Res.* **11**, 148–152.
- KAUSHIK, P., MONDAL, P.K. & CHAKRABORTY, S. 2016 Flow dynamics of a viscoelastic fluid squeezed and extruded between two parallel plates. *J. Non-Newtonian Fluid Mech.* **227**, 56–64.
- KOKINI, J.L. 1987 The physical basis of liquid food texture and texture-taste interactions. *J. Food Engng* **6**, 51–81.
- KUZMA, D.C. 1967 Fluid inertia effects in squeeze films. *Appl. Sci. Res.* **18**, 15–20.
- LEIDER, P.J. 1974 Squeezing flow between parallel disks ii: experimental results. *Ind. Engng Chem. Res.* **13**, 342–346.
- LEIDER, P.J. & BIRD, R.B. 1974 Squeezing flow between parallel disks i: theoretical analysis. *Ind. Engng Chem. Res.* **13**, 336–341.
- LIAN, G., XU, Y., HUANG, W. & ADAMS, M.J. 2001 On the squeeze flow of a power-law fluid between rigid spheres. *J. Non-Newtonian Fluid Mech.* **100**, 151–164.
- LUKEY, B.J., ROMANO, J.A. & SALEM, H. 2007 *Chemical Warfare Agents: Chemistry, Pharmacology, Toxicology, and Therapeutics*. CRC Press.
- MAUDE, A.D. 1961 End effects in a falling-sphere viscometer. *Brit. J. Appl. Phys.* **12**, 293–295.
- MEETEN, G.H. 2005 Flow of soft solids squeezed between planar and spherical surfaces. *Rheol. Acta* **44**, 563–572.
- MEZGER, T.G. 2006 *The Rheology Handbook*. Vincentz Network GmbH & Co KG.
- MOGHISI, M. & SQUIRE, P.T. 1981 An experimental investigation of the initial force of impact on a sphere striking a liquid surface. *J. Fluid Mech.* **108**, 133–146.
- MOSS, E.A., KRASSNOKUTSKI, A., SKEWS, B.W. & PATON, R.T. 2011 Highly transient squeeze-film flows. *J. Fluid Mech.* **671**, 384–398.
- PHAN-THIEN, N., SUGENG, F. & TANNER, R.I. 1987 The squeeze-film flow of a viscoelastic fluid. *J. Non-Newtonian Fluid Mech.* **24**, 97–119.
- PHAN-THIEN, N. & TANNER, R.I. 1984 Lubrication squeeze-film theory for the Oldroyd-B fluid. *J. Non-Newtonian Fluid Mech.* **14**, 327–335.
- POLYANIN, A.D. & ZAITSEV, V.F. 2003 *Handbook of Exact Solutions for Ordinary Differential Equations*, 2nd edn, p. 336. Chapman & Hall / CRC Press.
- RASHIDI, M.M., SHAHMOHAMADI, H. & DINARVAND, S. 2008 analytic approximate solutions for unsteady two-dimensional and axisymmetric squeezing flows between parallel plates. *Math. Probl. Engng* **2008**, 935095.
- RODIN, G.J. 1996 Squeeze film between two spheres in a power-law fluid. *J. Non-Newtonian Fluid Mech.* **63**, 141–152.
- SEGUR, J.B. & OBERSTAR, H.E. 1951 Viscosity of glycerol and its aqueous solutions. *Ind. Engng Chem.* **43**, 2117–2120.
- SHERWOOD, J.D. 2011 Squeeze flow of a power-law fluid between non-parallel plates. *J. Non-Newtonian Fluid Mech.* **166**, 289–296.
- SHIFFMAN, M. & SPENCER, D.C. 1945 The force of impact on a sphere striking a water surface. *Applied Mathematics Panel Report* 42.1R. Applied Mathematics Group.
- SIJS, R. & BONN, D. 2020 The effect of adjuvants on spray droplet size from hydraulic nozzles. *Pest Manage. Sci.* **76**, 3487–3494.
- TICHY, J.A. 1981 An approximate analysis of fluid inertia effects in axisymmetric laminar squeeze film flow at arbitrary Reynolds number. *Appl. Sci. Res.* **37** (3–4), 301–312.
- TICHY, J.A. & MODEST, M.F. 1978 Squeeze film flow between arbitrary two-dimensional surfaces subject to normal oscillations. *Trans. ASME J. Lubr. Technol.* **100** (3), 316–322.
- UDDIN, J., MARSTON, J.O. & THORODDSSEN, S.T. 2002 Squeeze flow of a Carreau fluid during sphere impact. *Phys. Fluids* **24**, 073104.
- USHA, R. & VIMALA, P. 2002 Curved squeeze film with inertial effects - energy integral approach. *Fluid Dyn. Res.* **30**, 139–153.
- VELTKAMP, B., VELIKOV, K.P. & BONN, D. 2022 Lubrication with non-Newtonian fluids. *Phys. Rev. Appl.* (under review).
- VELTKAMP, B., VELIKOV, K.P., VENNER, C.H. & BONN, D. 2021 Lubricated friction and the Hersey number. *Phys. Rev. Lett.* **126**, 044301.
- VENNER, C.H. & LUBRECHT, A.A. 2000 *Multilevel Methods in Lubrication*. Elsevier.